

Biocatalytic oligomerization of azoles; experimental and computational studies – supplementary material

Contents

| | |
|---|-------------|
| HPLC conditions | page 2 |
| pH optimization of 2-AI, 2-ABI, 3-AP and 4-AAP | page 3 |
| pH optimization of HOBT, 2-AT and 2-ABT | page 4 |
| pH optimization of pyrrole and indole | page 5 |
| Effect of enzyme activity on transformation of 2-AI and 2-ABI | page 5 |
| Effect of enzyme activity on transformation of 3-AP, 4-AAP and HOBT | page 6 |
| Effect of enzyme activity on transformation of 2-AT, 2-ABT, indole and pyrrole | page 7 |
| Effect of enzyme activity on pyrrole transformation in higher enzyme activities | page 8 |
| Effect of H ₂ O ₂ concentration on transformation of 2-AI and 2-ABI | page 8 |
| Effect of H ₂ O ₂ concentration of transformation of 3-AP, 4-AAP and HOBT | page 9 |
| Effect of H ₂ O ₂ on transformation of 2-AT, 2-ABT, indole and pyrrole | page 10 |
| Time dependence of 2-AI and 2-ABI transformations | page 11 |
| Time dependence of 3-AP and 4-AAP transformations | page 12 |
| Time dependence of HOBT transformation | page 13 |
| Time dependence of 2-AT and 2-ABT transformations | page 14 |
| Time dependence of pyrrole and indole transformations | page 15 |
| Spin density analysis | pages 16-18 |
| Spin densities for non-substrates graphic | page 19 |
| Spin densities calculated for all compounds | pages 19-24 |
| Identification of products by mass spectrometry, discussion and structural figures | |
| 2-AI and 2-ABI | pages 25-27 |
| 3-AP and 4-AAP | pages 27-30 |
| HOBT | pages 31-32 |
| 2-AT and 2-ABT | pages 32-36 |
| Pyrrole | pages 37-38 |
| Indole | pages 38-40 |
| References | page 41 |

Table S1. HPLC conditions for substrates run under gradient elution

| Substrate | Time (min) | Flow mL/min | Mobile phase ratio | | λ_{\max} nm |
|-----------|------------|-------------|--------------------|----------|---------------------|
| | | | Pump A* | Pump B** | |
| HOBT | 0 | 1.0 | 90% | 10% | 305 |
| | 3.5 | 1.0 | 5% | 95% | |
| | 8 | 1.0 | 5% | 95% | |
| | 9 | 1.0 | 90% | 10% | |
| | 25 | 1.0 | 90% | 10% | |
| 2-AI | 0 | 0.60 | 90% | 10% | 210 |
| | 2 | 0.60 | 5% | 95% | |
| | 8 | 0.60 | 5% | 95% | |
| | 9 | 0.60 | 90% | 10% | |
| | 15 | 0.60 | 90% | 10% | |

* Pump A: 0.1% H_3PO_4

**Pump B: ACN+ 0.1% H_3PO_4

Table S2. HPLC conditions for substrates run under isocratic elution

| Substrate | Mobile phase ratio | | Flow mL/min | λ_{\max} nm | Column |
|-----------|----------------------------|---------|-------------|---------------------|----------|
| | Pump A | Pump B | | | |
| Pyrrole | 30% formic acid (0.1%) | 70% ACN | 0.54 | 210 | Symmetry |
| Indole | 20% formic acid (0.1%) | 80% ACN | 0.60 | 269 | Symmetry |
| 3-AP | 50% formic acid (0.1%) | 50% ACN | 0.40 | 230 | PS |
| 4-AAP | 50% ammonium acetate (5mM) | 50% ACN | 0.40 | 244 | HILIC |
| 2-ABI | 70% formic acid (0.1%) | 30% ACN | 0.30 | 280 | Symmetry |
| 2-AT | 50% formic acid (0.1%) | 50% ACN | 0.6 | 254 | PS |
| 2-ABT | 50% formic acid (0.1%) | 50% ACN | 0.5 | 258 | PS |

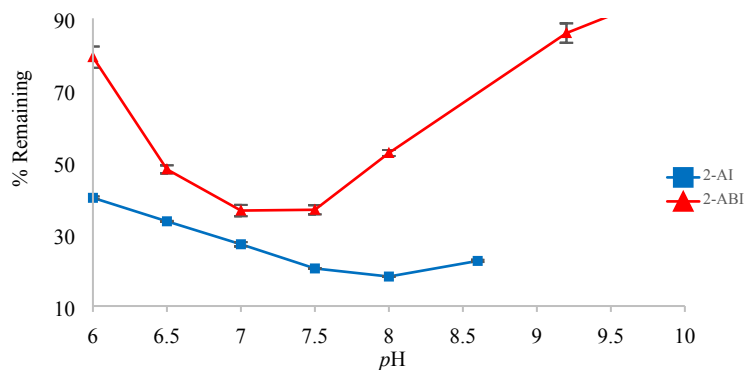


Figure S1. pH optimization of 2-AI and 2-ABI.

Conditions for 0.5 mM 2-AI: 10 mM respective buffer, 1.5 U/mL SBP and 0.75 mM H₂O₂. Conditions for 0.5 mM 2-ABI: 40 mM respective buffer, 1.5 U/mL SBP and 0.75 mM H₂O₂. (For 2-AI, a lower buffer concentration, 10 mM, was used to avoid the interference of buffer absorbance in the UV-Vis range in which 2-AI absorbs.)

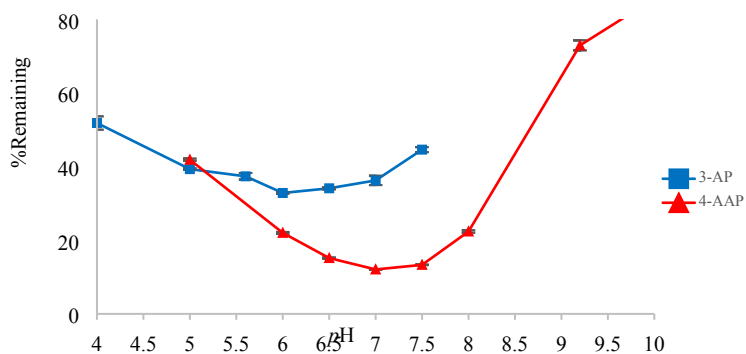


Figure S2. pH optimization of 3-AP and 4-AAP

Conditions for 1.0 mM 3-AP: 10 mM respective buffer, 1.7 U/mL SBP and 1.5 mM H₂O₂. Conditions for 0.5 mM 4-AAP: 40 mM respective buffer, 1.5 U/mL SBP and 1.0 mM H₂O₂. (For 2-AI, a lower buffer concentration, 10 mM, was used to avoid the interference of buffer absorbance in the UV-Vis range in which 3-AP absorbs.)

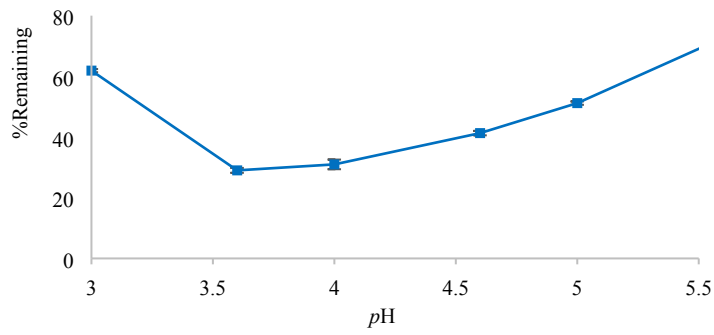


Figure S3. pH optimization of HOBT

Conditions for 1.0 HOBT: 40 mM respective buffer, 0.03 U/mL SBP and 1.5 mM H₂O₂

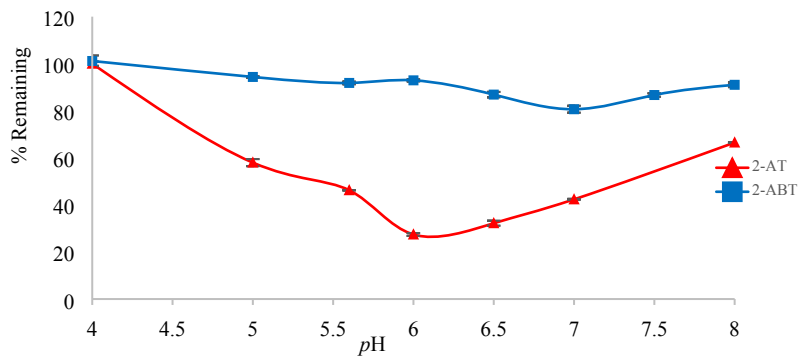


Figure S4. pH optimization of 2-AT and 2-ABT

Conditions for 1.0 mM 2-AT: 40 mM respective buffer, 3.0 U/mL SBP and 2.0 mM H₂O₂. Conditions for 0.5 mM 2-ABT: 40 mM respective buffer, 1.5 U/mL SBP and 0.75 mM H₂O₂.

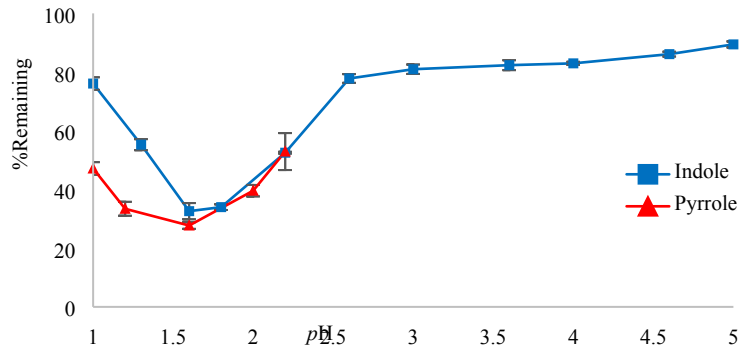


Figure S5. pH optimization of pyrrole and indole

Conditions for 1.0 mM pyrrole: 40 mM buffer, 1.5 mM H_2O_2 and 3.0 U/mL SBP. For 1.0 mM indole conditions: 40 mM buffer, 1.5 mM H_2O_2 and 0.25 U/mL SBP.

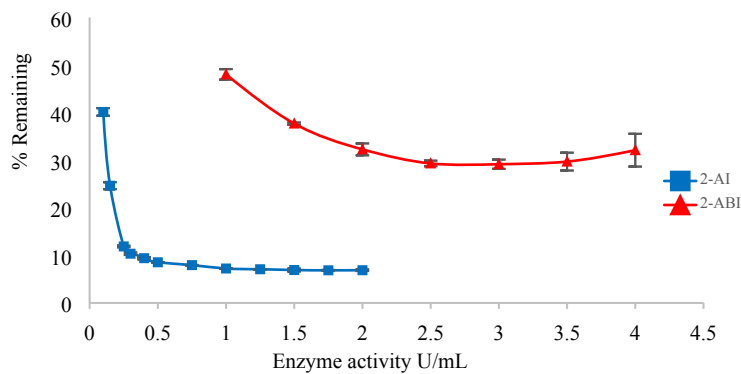


Figure S6. Effect of enzyme activity on transformation of 2-AI and 2-ABI.

Conditions for 0.5 mM 2-AI: 10 mM pH 8.0 buffer, 1.0 mM H_2O_2 . For 0.5 mM 2-ABI conditions: 40 mM pH 7.0 buffer, 0.75 mM H_2O_2 .

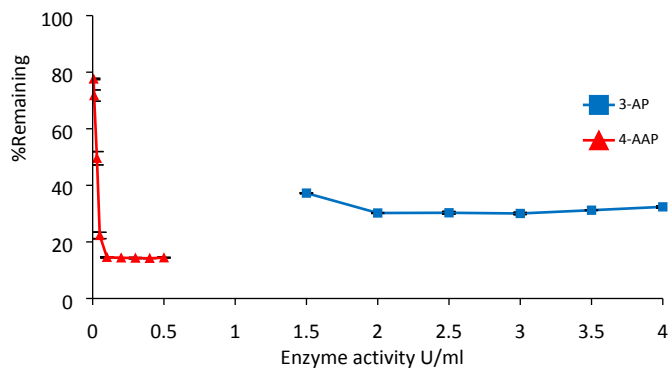


Figure S7. Effect of enzyme activity on transformation of 3-AP and 4-AAP.

Conditions for 1.0 mM 3-AP: 10 mM pH 6.0 buffer, 1.5 mM H₂O₂. For 0.5 mM 4-AAP conditions: 40 mM pH 7.5 buffer, 1.0 mM H₂O₂.

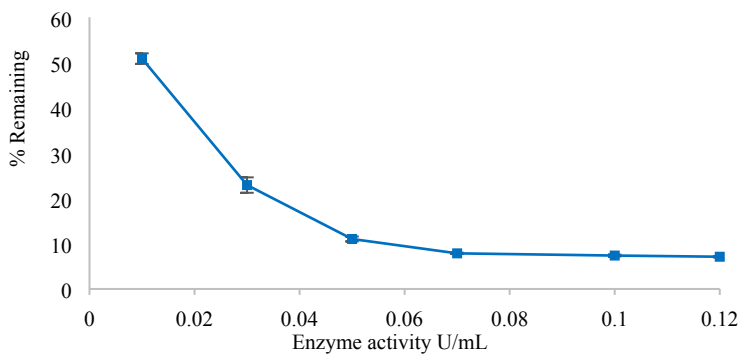


Figure S8. Effect of enzyme activity on transformation of HOBT.

Conditions for 1.0 mM HOBT: 40 mM pH 3.6 buffer, 1.5 mM H₂O₂.

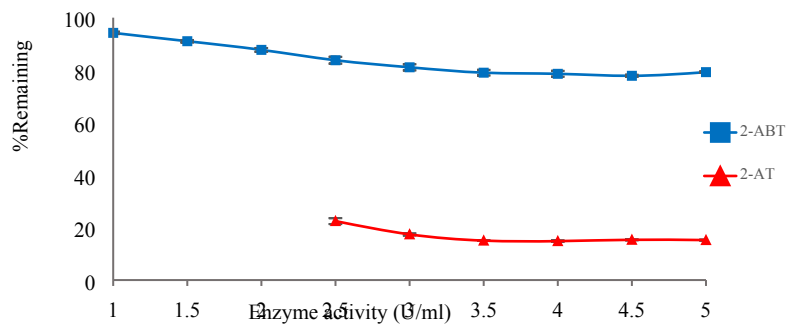


Figure S9. Effect of enzyme activity on transformation of 2-AT and 2-ABT

Conditions for 1.0 mM 2-AT: 40 mM pH 6.0 buffer, 2.0 mM H_2O_2 . For 0.5 mM 2-ABT conditions: 40 mM pH 7.0 buffer, 0.75 mM H_2O_2 .

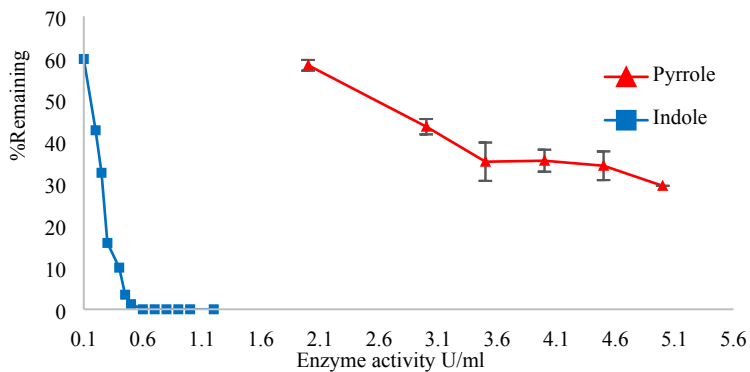


Figure S10. Effect of enzyme activity on transformation of indole and pyrrole

Conditions for 1.0 mM pyrrole: 40 mM pH 1.6 buffer, 1.5 mM H_2O_2 . For 1.0 mM indole conditions: 40 mM pH 1.6 buffer, 1.5 mM H_2O_2 .

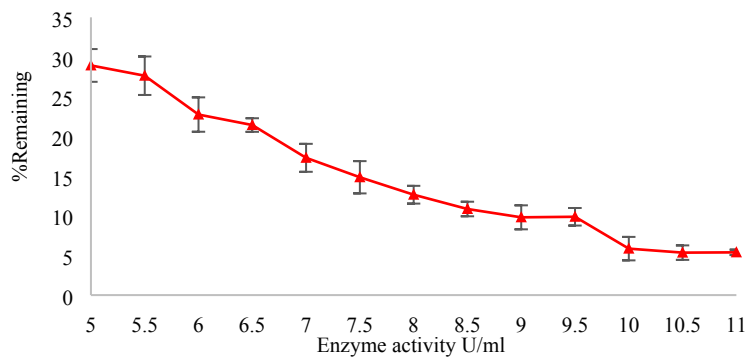


Figure S11. Effect of enzyme activity on pyrrole transformation in higher enzyme activities

Conditions for 1.0 mM pyrrole: 40 mM pH 1.6 buffer, 1.5 mM H₂O₂

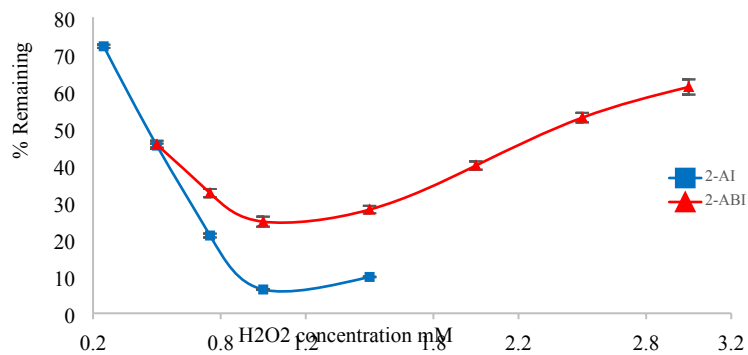


Figure S12. Effect of H₂O₂ concentration on transformation of 2-AI and 2-ABI.

Conditions for 0.5 mM 2-AI: 10 mM pH 8.0 buffer, 1.5 U/mL SBP. For 0.5 mM 2-ABI, conditions: 40 mM pH 7.0 buffer, 3.0 U/mL SBP.

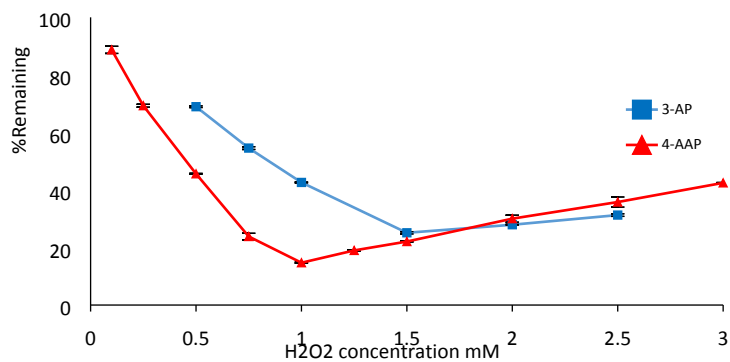


Figure S13. Effect of H₂O₂ concentration of transformation of 3-AP and 4-AAP.

Conditions for 1.0 mM 3-AP: 10 mM pH 6.0 buffer, 3.0 U/mL SBP. For 0.5 mM 4-AAP, conditions: 40 mM pH 7.5 buffer, 0.1 U/mL SBP.

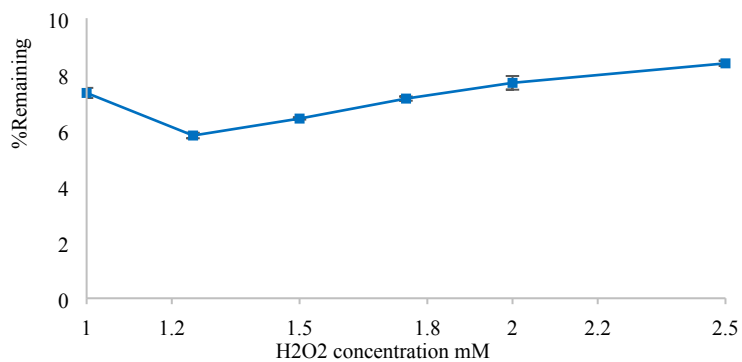


Figure S14. Effect of H₂O₂ on transformation of HOBT.

Conditions for 1.0 mM HOBT: 40 mM pH 3.6 buffer, 0.125 U/mL SBP.

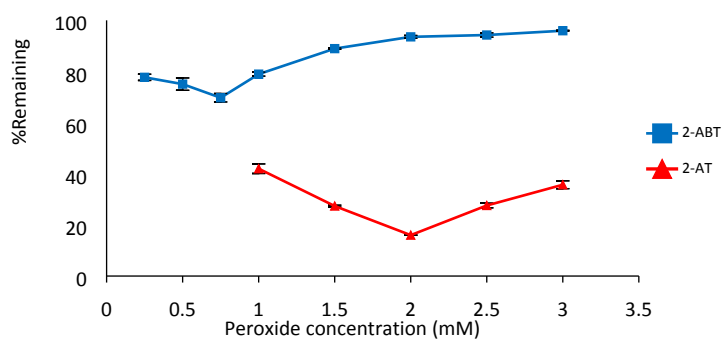


Figure S15. Effect of H_2O_2 on transformation of 2-AT and 2-ABT

Conditions for 1.0 mM 2-AT: 40 mM pH 6.0 buffer, 4.5 U/mL SBP. For 0.5 mM 2-ABT, conditions: 40 mM pH 7.0 buffer, 5.0 U/mL SBP.

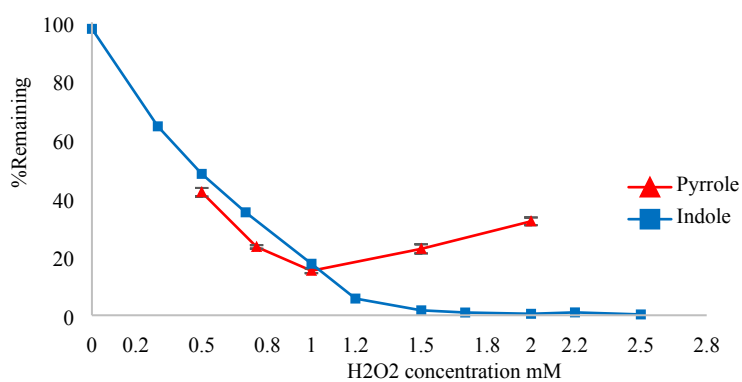


Figure S16. Effect of H_2O_2 on transformation of indole and pyrrole

Conditions for 1.0 mM pyrrole: 40 mM pH 1.6 buffer and 5.0 U/mL SBP. For 1.0 mM indole conditions: 40 mM pH 1.6 buffer and 0.45 U/mL SBP.

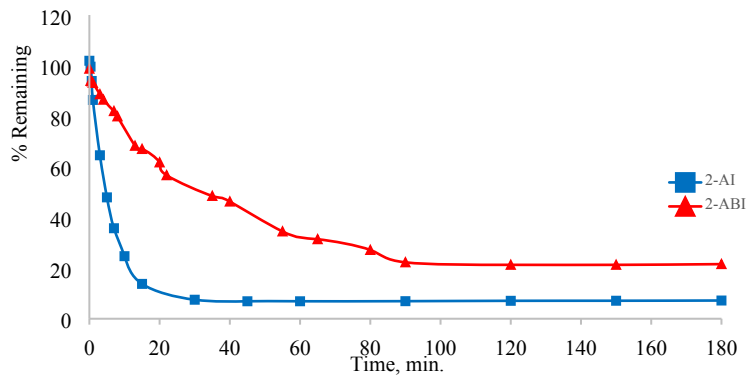


Figure S17. Time dependence of imidazole transformations.

For 0.5 mM 2-AI conditions: 40 mM pH 8.0 buffer, 1.5 U/mL SBP and 1.0 mM H₂O₂. For 0.5 mM 2-ABI, conditions: 40 mM pH 7.0 buffer, 3.0 U/mL SBP and 1.0 mM H₂O₂.

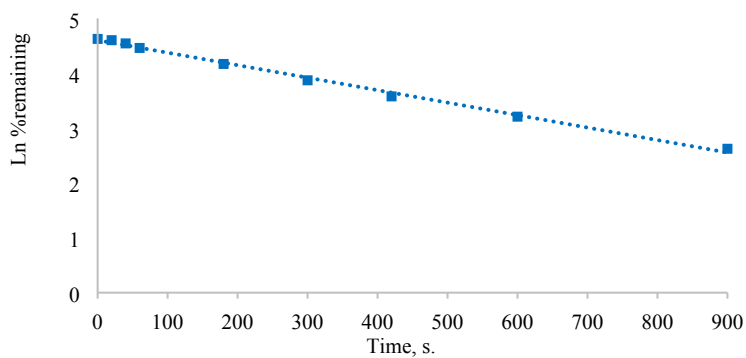


Figure S18. First-order loss of 2-AI at the beginning of the reaction. Data from figure S17.

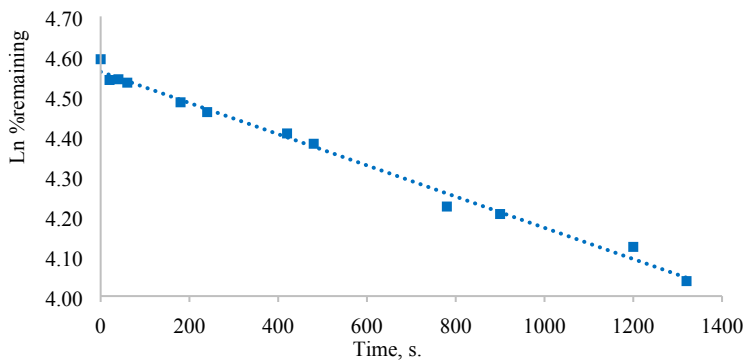


Figure S19. First-order loss of 2-ABI at the beginning of the reaction. Data from figure S17.

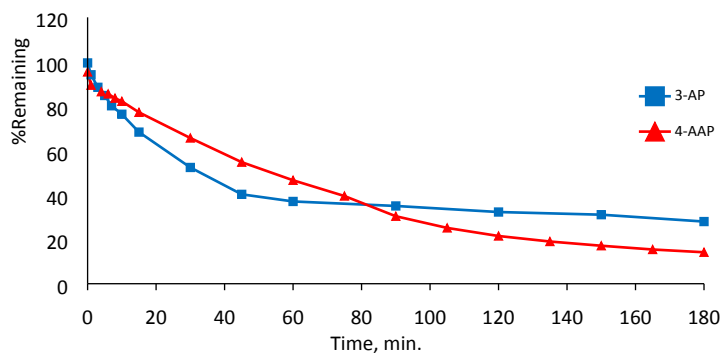


Figure S20. Time dependence of pyrazole transformations.

For 1.0 mM 3-AP conditions: 10 mM pH 6.0 buffer, 3.0 U/mL SBP and 1.5 mM H₂O₂. For 0.5 mM 4-AAP, conditions: 40 mM pH 7.5 buffer, 0.1 U/mL SBP and 1.0 mM H₂O₂.

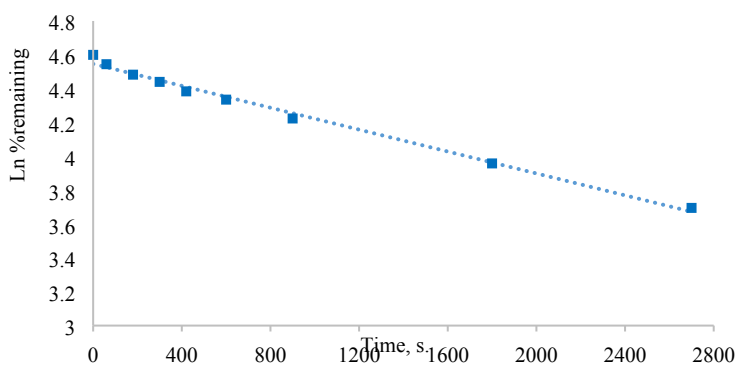


Figure S21. First-order loss of 3-AP at the beginning of the reaction. Data from Figure S20.

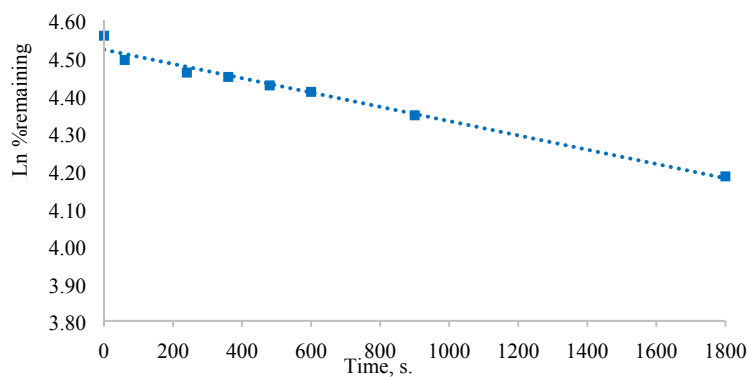


Figure S22. First-order loss of 4-AAP at the beginning of the reaction. Data from Figure S20.

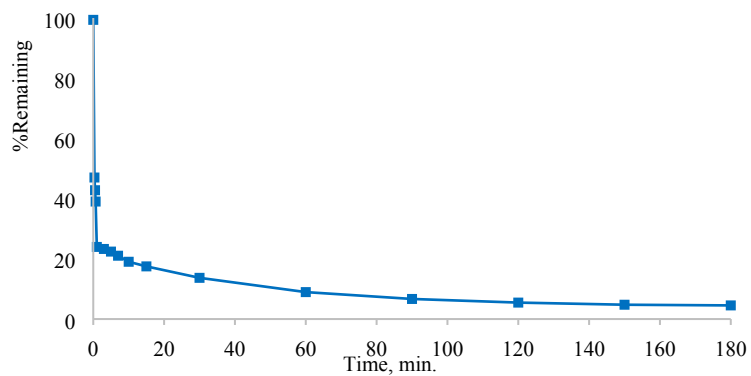


Figure S23. Time dependence of HOBT transformation.

Conditions for 1.0 mM HOBT: 40 mM pH 3.6 buffer, 0.12 U/mL SBP and 1.25 mM H₂O₂

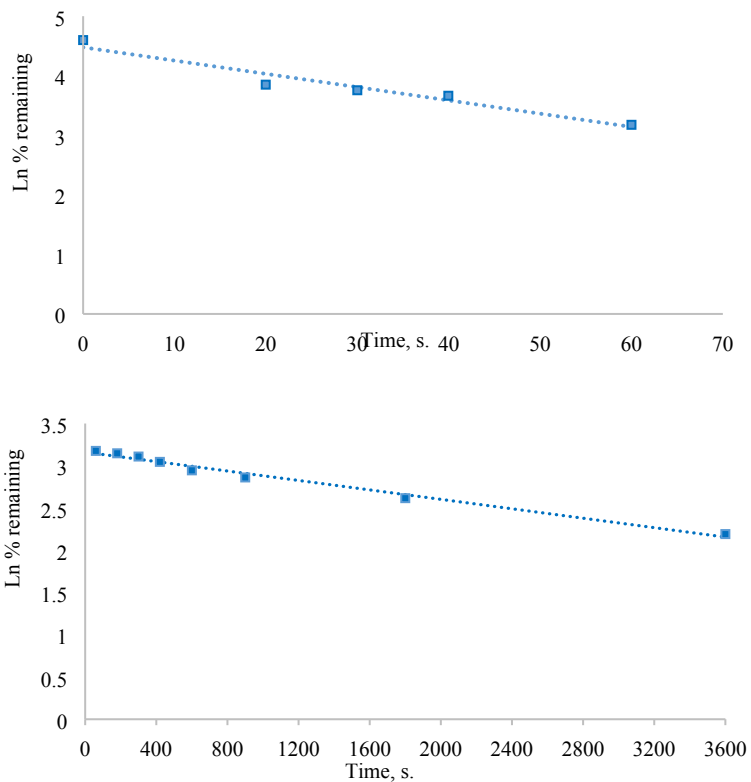


Figure S24. First-order loss of HOBT at the beginning of the reaction, fast and slow phases. Data from Figure S23.

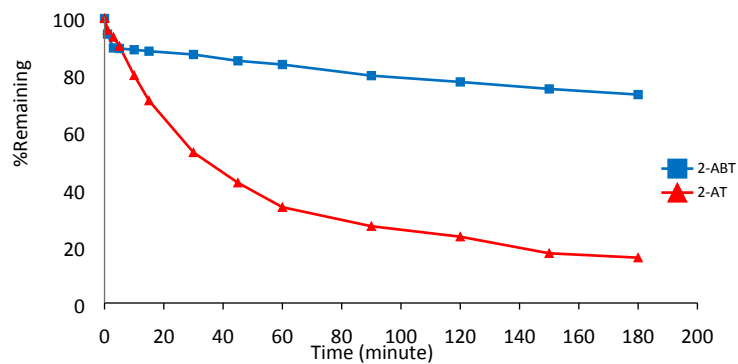


Figure S25. Time dependence of thiazoles transformation

For 1.0 mM 2-AT conditions: 40 mM pH 6.0 buffer, 4.0 U/mL SBP and 1.5 mM H₂O₂. For 0.5 mM 2-ABT, conditions: 40 mM pH 7.0 buffer, 4.5 U/mL SBP and 0.75 mM H₂O₂.

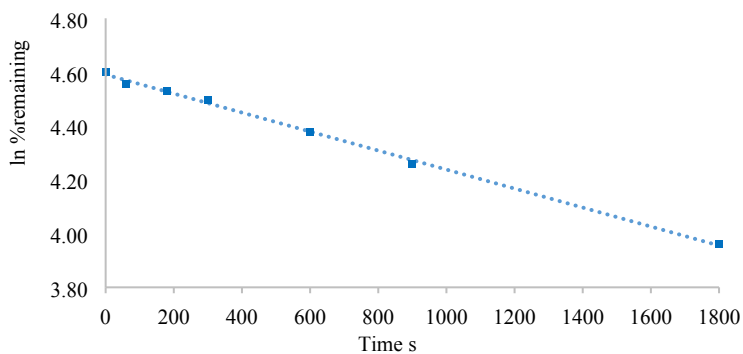


Figure S26. First-order loss of 2-AT at the beginning of the reaction. Data from Figure S25.

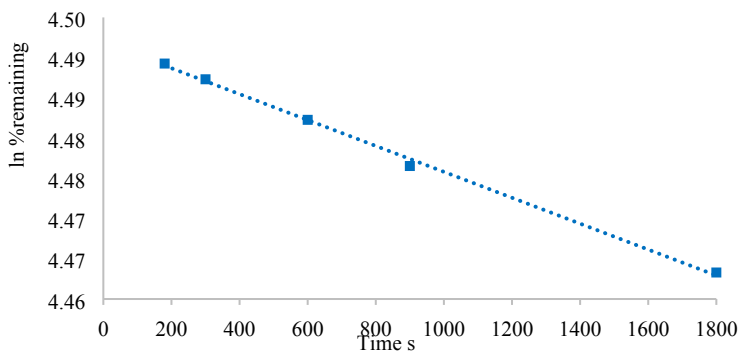


Figure S27. First-order loss of 2-ABT at the beginning of the reaction. Data from Figure S25.

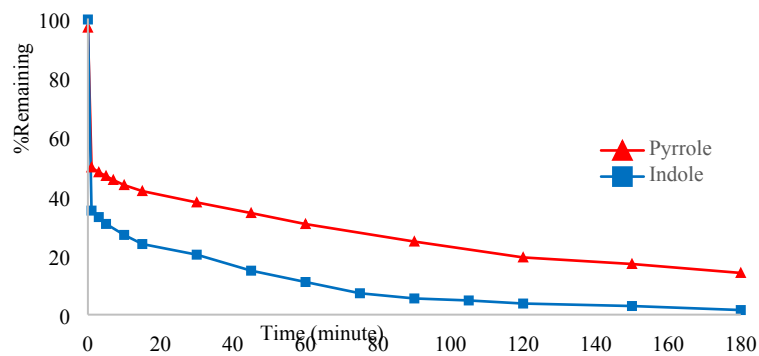


Figure S28. Time dependence of pyrrole and indole transformation

Conditions for 1.0 mM pyrrole: 40 mM pH 1.6 buffer, 1.5 mM H_2O_2 and 5.0 U/mL SBP. For 1.0 mM indole conditions: 40 mM pH 1.6 buffer, 1.25 mM H_2O_2 and 0.45 U/mL SBP.

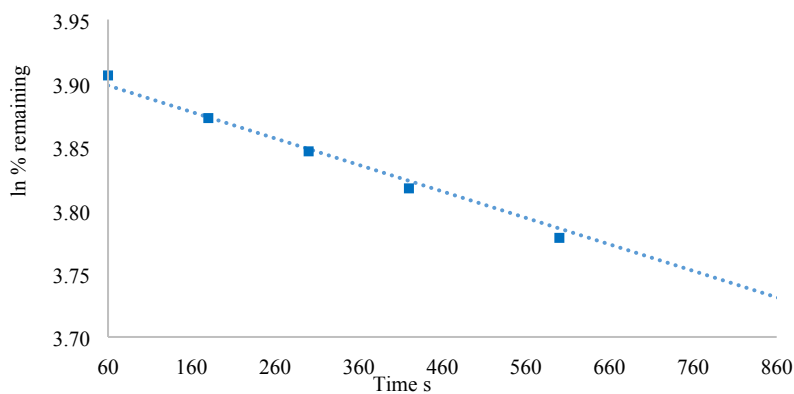


Figure S29. First-order loss of pyrrole at the beginning of the reaction (slow phase). Data from Figure S28.

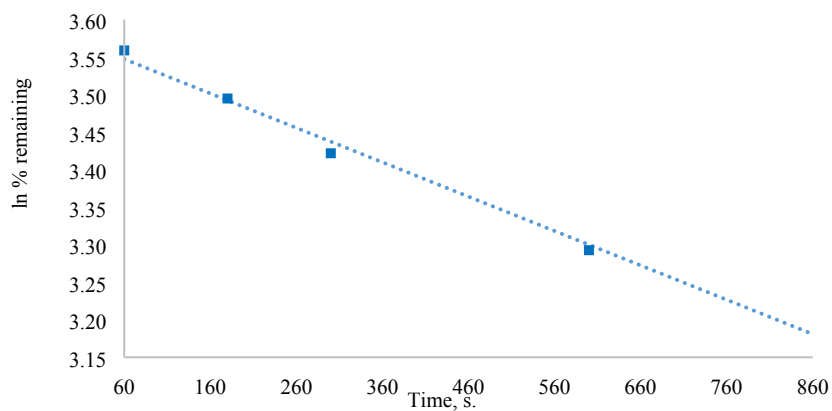


Figure S30. First-order loss of indole at the beginning of the reaction (slow phase). Data from Figure S28.

Spin density analysis

The highest spin densities for the non-substrates are summarized in Figure S31; the corresponding summary for substrates is in Figure 1. Complete tables (Tables S3 – S19) of calculated spin densities for all compounds are given following this discussion of the calculated values. For symmetrical imidazole radical (spin values, Table S3) the highest spin value is on C-2. Positive spin densities are localized only on the carbon atoms. For imidazole radical cation (loss of an electron but not a proton), carbon atoms also have positive spin values (data not shown) consistent with previously reported spin values for imidazole radical cation (Kinsley and Nicell, 2000). For 2-AI radical (Table S4) highest spin values are on the exocyclic nitrogen and C-5 while the pyrrole-type nitrogen of the ring shows much higher spin value than the pyridine-type nitrogen. The highest spin values for 2-ABI radical are localized on the exocyclic nitrogen, pyridine-type endocyclic nitrogen and C-3a (Table S5).

Based on the spin distribution patterns in 2-AI and 2-ABI radicals, N-N coupling through the exocyclic nitrogen is very probable and was confirmed by MS evidence (see below) for azo-dimers in both cases. Spin density is distributed symmetrically over the pyrazole radical, C-3 and C-5 have equal large spin values while both nitrogens have equal, much smaller spin values (Table S6). For the 3-AP radical, the exocyclic nitrogen has the highest spin value. In the ring, the pyridine-type nitrogen, shows higher spin value than the pyrrole-type nitrogen (Table S7). Spin density of 4-AAP (Table S8) is only delocalized over the heterocyclic ring; as expected, the exocyclic nitrogen carries the highest spin density. The second-highest spin value is on C-3 which is not expected to participate in the coupling reaction due to steric effects and the disruption of aromaticity in the coupling product. For the pyrazoles, highest spin values are on the exocyclic nitrogen, thus, formation of azo-oligomers is highly probable for 3-AP and 4-AAP,

consistent with MS analysis. In the HOBT radical, spin density is only localized on the oxygen atom plus N-1 and N-3 of the heterocyclic ring, (Table S9), suggesting the possibility of N-N, N-O and O-O coupling. Unlike HOBT radical, in HOBT radical cation the spin density is delocalized over whole molecule with C-7 and C-5 of the benzene ring having higher spin values than the heteroatoms (data not shown).

The spin values calculated for the loss of an electron and a proton from thiophene, indicated a spin value of almost 1 on C-2 (one of α -carbons) (Mukhopadhyay et al., 2017). For thiophene radical cation, spin is delocalized over the sulfur atom (0.66) and both α -carbons (0.32), confirming the previously reported formation of α -conjugated oligo- and poly-thiophenes (Lu et al., 2010). The spin density maps and calculated spin values for thiophenes, thiazoles, pyrrole and indole are presented in Tables S10-19.

In benzothiophene radical, the spin density is delocalized over C-3 (0.49), C-6 (0.17), C-2 (0.14) and S-1 (0.13). Similar to thiophene, the spin densities in thiazole and benzothiazole are predominantly localized on C-2 (0.91 and 0.83, respectively). Experimental and theoretical data collected for electro-polymerization of benzothiophene showed high spin delocalization on S-1, C-2, C-3, C-4, C-7, in accordance with experimental results from oligomer analysis which showed C-2, C-3 and C-7 as the most favored oligomerization sites (Çiftçi et al., 2013). No literature regarding the spin density distribution of thiazole and benzothiazole radicals were found for comparison. In the 2-AT radical, the spin density is delocalized over the whole molecule with the exocyclic nitrogen, C-5 and aza-nitrogen carrying the highest spin values. In 2-ABT radical, spin is delocalized over both aromatic rings with both nitrogens having comparable spin, in contrast to 2-AT. Position C-7a in 2-ABT shows high positive spin value but it is unlikely to participate in coupling due to steric hindrance and loss of aromatic stabilization

in any coupling product. Although 2-HBT was not a substrate of SBP, its spin distribution pattern was very similar to that of 2-ABT with the spin delocalized over both rings and oxygen and nitrogen atoms carrying positive values. The spin density in pyrrole radical is delocalized on the α -carbons. Previous studies using X-ray photon-electron spectrometry on polypyrrole film indicated α - α linkage as the main route of polymerization of pyrrole in addition to minor coupling through the α - β linkages (Li et al., 2016a) consistent with ab-initio calculations of relative stabilities of different oligomers which showed that the α - α linkage has the lowest bond energy (Yurtsever and Yurtsever, 1999). Indole radical has highest spin density on C-3 followed by nitrogen and C-4. An indole oligomer stability study has shown that although C-2 is a possible polymerization site, further polymer growth (due to low configuration energy and small torsional angle) is inhibited, hence C-3 and C-7 contribute to the formation of oligomer. In addition, it was stated that sterically and thermodynamically stable cyclic trimer and tetramers could be formed with six- and eight-membered rings in the center, respectively, with linkages through C-2 and C-3 and through C-6 and C-7 forming the most stable cyclic structures (Yurtsever and Yurtsever, 2002). Electron-rich and thermally-stable cyclic indole trimers (triazatruxene and isotriazatruxene, see Figure S37 (e)), have been synthesized from indole and 2-indolone, respectively (Li et al., 2016b). The possibility of formation of the above conjugated indole oligomers in this work is discussed below in identification of products by mass spectrometry. For the non-substrate indazole, N-1, C-3, C-7 and N-2 show the highest spin values.

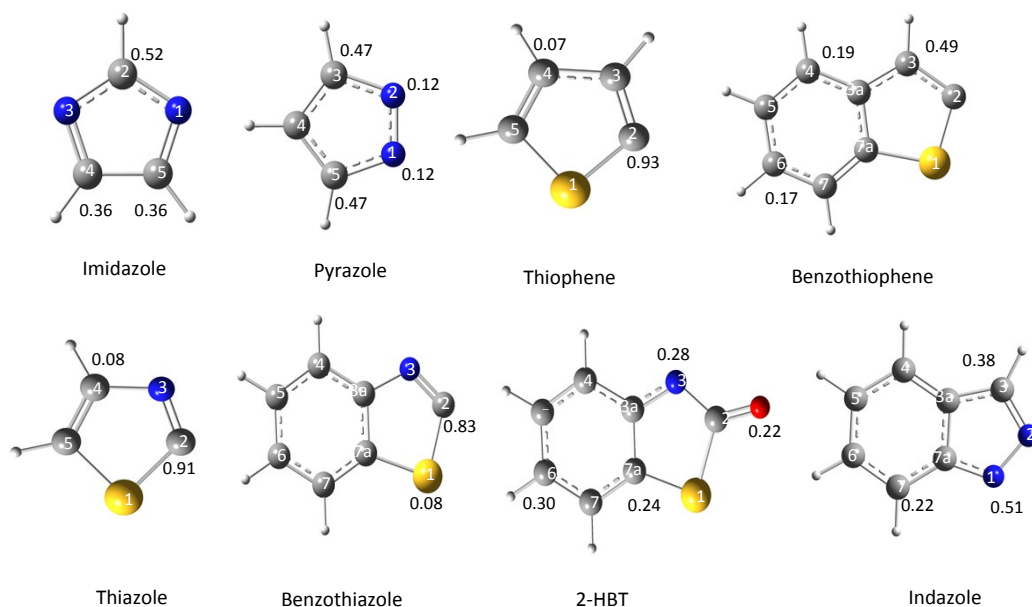


Figure S31. Highest spin densities calculated for the studied non-substrates reported in black and atom positions in white numbers. yellow represents sulfur, blue represents nitrogen and red represents oxygen atom.

Table S3. Calculated spin densities imidazole radical

| | Spin density |
|-----|--------------|
| N 1 | -0.12 |
| C 2 | 0.52 |
| N 3 | -0.12 |
| C 4 | 0.36 |
| C 5 | 0.36 |

Table S4. Calculated spin densities for 2-AI radical

| | Spin density |
|------|--------------|
| N 1 | 0.08 |
| C 2 | -0.12 |
| N 3 | 0.22 |
| C 4 | 0.02 |
| C 5 | 0.33 |
| N C2 | 0.46 |

Table S5. Calculated spin densities for 2-ABI radical

| | Spin density |
|------|--------------|
| N 1 | 0.31 |
| C 2 | -0.14 |
| N 3 | 0.05 |
| C 3a | 0.27 |
| C 4 | -0.07 |
| C 5 | 0.19 |
| C 6 | -0.01 |
| C 7 | 0.02 |
| C 7a | -0.06 |
| N C2 | 0.43 |

Table S6. Calculated spin densities for pyrazole radical

| | Spin density |
|-----|--------------|
| N 1 | 0.12 |
| N 2 | 0.12 |
| C 3 | 0.47 |
| C 4 | -0.18 |
| C 5 | 0.47 |

Table S7. Calculated spin densities for 3-AP radical

| | Spin density |
|------|--------------|
| N 1 | 0.15 |
| N 2 | 0.32 |
| C 3 | -0.18 |
| C 4 | 0.19 |
| C 5 | -0.09 |
| N C3 | 0.62 |

Table S8. Calculated spin densities for 4-AAP radical

| | Spin density |
|------|--------------|
| N 1 | 0.00 |
| N 2 | 0.10 |
| C 3 | 0.35 |
| C 4 | -0.13 |
| C 5 | 0.06 |
| N C4 | 0.55 |
| O C5 | 0.06 |
| C 1' | 0.01 |
| C 2' | -0.01 |
| C 3' | 0.00 |
| C 4' | 0.00 |
| C 5' | 0.01 |
| C 6' | 0.01 |

Table S9. Calculated spin densities for HOBT radical

| | Spin density |
|------|--------------|
| N 1 | 0.21 |
| N 2 | -0.06 |
| N 3 | 0.21 |
| C 3a | 0.00 |
| C 4 | 0.01 |
| C 5 | 0.05 |
| C 6 | -0.01 |
| C 7 | 0.08 |
| C 7a | -0.04 |
| O C1 | 0.55 |

Table S10. Calculated spin densities for thiophene radical

| | Spin density |
|-----|--------------|
| S 1 | 0.00 |
| C 2 | 0.93 |
| C 3 | -0.01 |
| C 4 | 0.07 |
| C 5 | 0.00 |

Table S 11. Calculated spin densities for benzothiophene radical

| | Spin density |
|------|--------------|
| S 1 | 0.13 |
| C 2 | 0.14 |
| C 3 | 0.49 |
| C 3a | -0.15 |
| C 4 | 0.19 |
| C 5 | -0.07 |
| C 6 | 0.17 |
| C 7 | 0.01 |
| C 7a | 0.08 |

Table S12. Calculated spin densities for thiazole radical

| | Spin density |
|-----|--------------|
| S 1 | 0.05 |
| C 2 | 0.91 |
| N 3 | 0.04 |
| C 4 | 0.08 |
| C 5 | 0.00 |

Table S13. Calculated spin densities for benzothiazole radical

| | Spin density |
|------|--------------|
| S 1 | 0.08 |
| C 2 | 0.83 |
| N 3 | -0.03 |
| C 3a | 0.07 |
| C 4 | 0.00 |
| C 5 | 0.00 |
| C 6 | -0.01 |
| C 7 | 0.03 |
| C 7a | 0.03 |

Table S14. Calculated spin densities for 2-AT radical

| | Spin density |
|------|--------------|
| S 1 | 0.15 |
| C 2 | -0.15 |
| N 3 | 0.26 |
| C 4 | -0.05 |
| C 5 | 0.39 |
| N C2 | 0.40 |

Table S15. Calculated spin densities for 2-ABT radical

| | Spin density |
|------|--------------|
| S 1 | 0.07 |
| C 2 | -0.17 |
| N 3 | 0.36 |
| C 3a | -0.10 |
| C 4 | 0.11 |
| C 5 | -0.05 |
| C 6 | 0.22 |
| C 7 | -0.11 |
| C 7a | 0.26 |
| N C2 | 0.41 |

Table S16. Calculated spin densities for 2-HBT radical

| | Spin density |
|------|--------------|
| S 1 | 0.03 |
| C 2 | -0.02 |
| N 3 | 0.28 |
| C 3a | 0.01 |
| C 4 | 0.15 |
| C 5 | -0.07 |
| C 6 | 0.30 |
| C 7 | -0.13 |
| C 7a | 0.24 |
| O C2 | 0.22 |

Table S17. Calculated spin densities for pyrrole radical

| | Spin density |
|-----|--------------|
| N 1 | -0.17 |
| C 2 | 0.50 |
| C 3 | 0.08 |
| C 4 | 0.08 |
| C 5 | 0.50 |

Table S18. Calculated spin densities for indole radical

| | Spin density |
|------|--------------|
| N 1 | 0.23 |
| C 2 | -0.05 |
| C 3 | 0.57 |
| C 3a | -0.90 |
| C 4 | 0.21 |
| C 5 | -0.05 |
| C 6 | 0.16 |
| C 7 | -0.01 |
| C 7a | 0.03 |

Table S19. Calculated spin densities for indazole radical

| | Spin density |
|------|--------------|
| N 1 | 0.51 |
| N 2 | 0.17 |
| C 3 | 0.38 |
| C 3a | 0.06 |
| C 4 | 0.03 |
| C 5 | 0.17 |
| C 6 | -0.06 |
| C 7 | 0.22 |
| C 7a | -0.15 |

Identification of products by mass spectrometry

This detailed discussion of the MS analyses includes of Figures 2-4 of the main manuscript; those figures are duplicated here for ease of reference to the discussion.

Imidazoles

ASAP (atmospheric solids analysis probe) analysis conducted on 2-AI standard showed the radical cation $[M]^+$, protonated standard $[M]$ and its ^{13}C -isotope. The mass spectrum of the of 2-AI enzymatic reaction supernatant revealed the presence of two oxidative-dimers, Figure 2 (a) three isomers, and its oxidized form, the azo-dimer, Figure 2(b). ESI (electrospray ionization) analysis conducted on the same supernatant did not indicate the presence of an azo-dimer but the peaks related to the oxidative dimer and its ^{13}C -isotope were observed. In addition to the oxidative dimer, ESI analysis suggested the presence of a trimer consistent with the structure shown in Figure 2 (c). ESI-MS analysis of the reaction blank (containing everything except 2-AI) did not show the trimer peak, indicating it to be a product of enzymatic reaction. ASAP-MS analysis conducted on the precipitate of the reaction showed the presence of dimers and trimers but no higher oligomers; ESI-MS analysis on the precipitate confirmed the presence of a trimer, with plausible structures shown in Figure 2 (d), plus the trimer reported above in ESI-MS of the supernatant, Figure 2 (c). The structures proposed for Figures 2 (c) and (d) are consistent with N-C but not necessarily C-C coupling at the oxidative dimer stage. ASAP-MS analysis of the 2-ABI reaction supernatant (Figure S32) suggested the presence of protonated oxidative dimers (three coupling modes possible) and an azo-dimer. The presence of both types of dimers was confirmed using ESI-MS analysis of the 2-ABI supernatant which did not indicate the presence of any other oligomers in the solution. The ASAP and ESI-MS analyses of the precipitate confirmed the presence of both azo- and oxidative dimers observed in the supernatant.

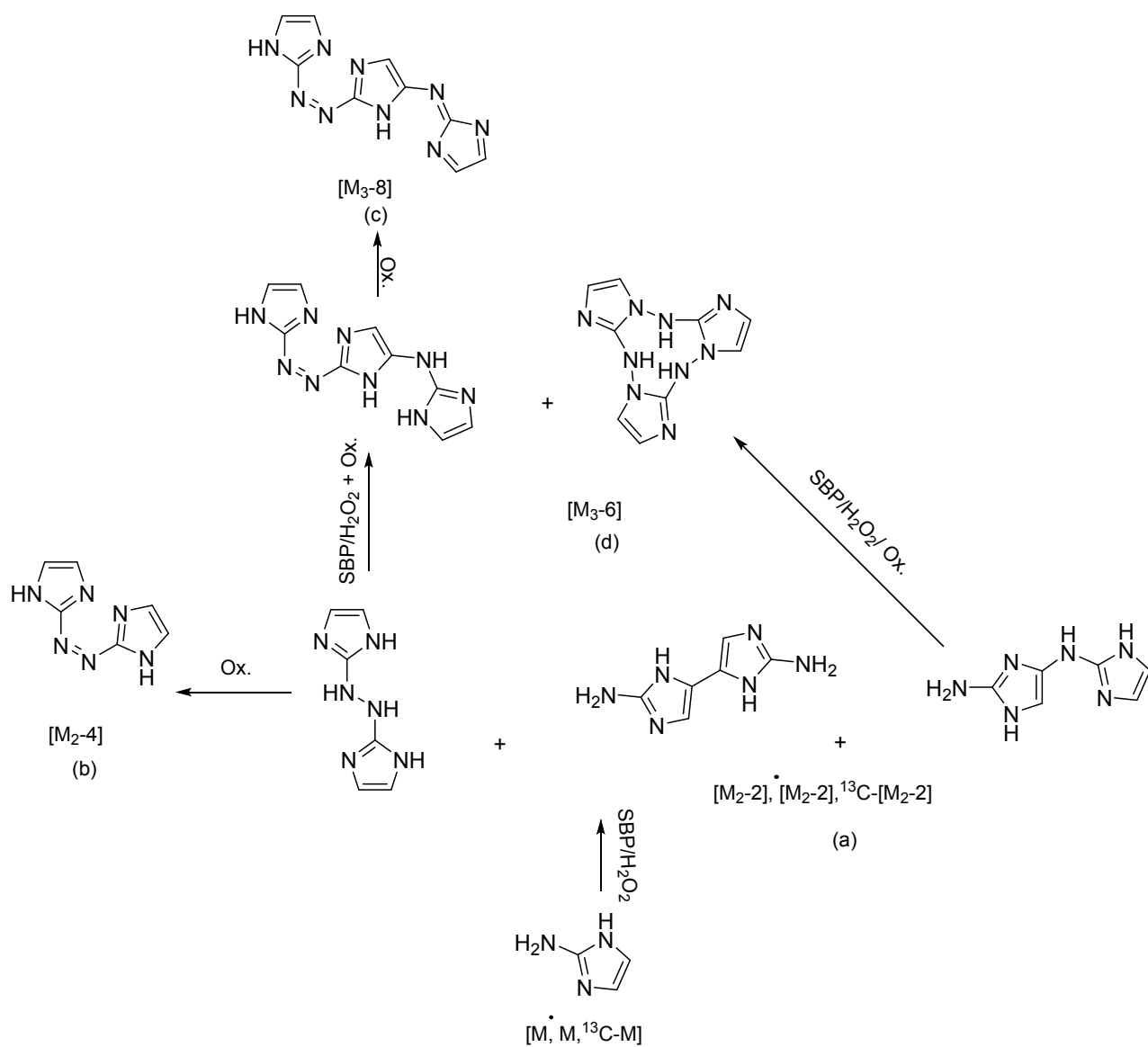


Figure 2. Proposed structures of oligomers generated from enzymatic treatment of 2-AI. In the symbolic labels, M^* is the parent monomer molecular radical cation, M is its protonated form, $^{13}C-M$ is the natural-abundance ^{13}C -isotope of the protonated monomer, M_2-2 is a protonated oxidative dimer, M_2-4 is a protonated oxidized oxidative dimer (such as an azo-dimer), and so on.

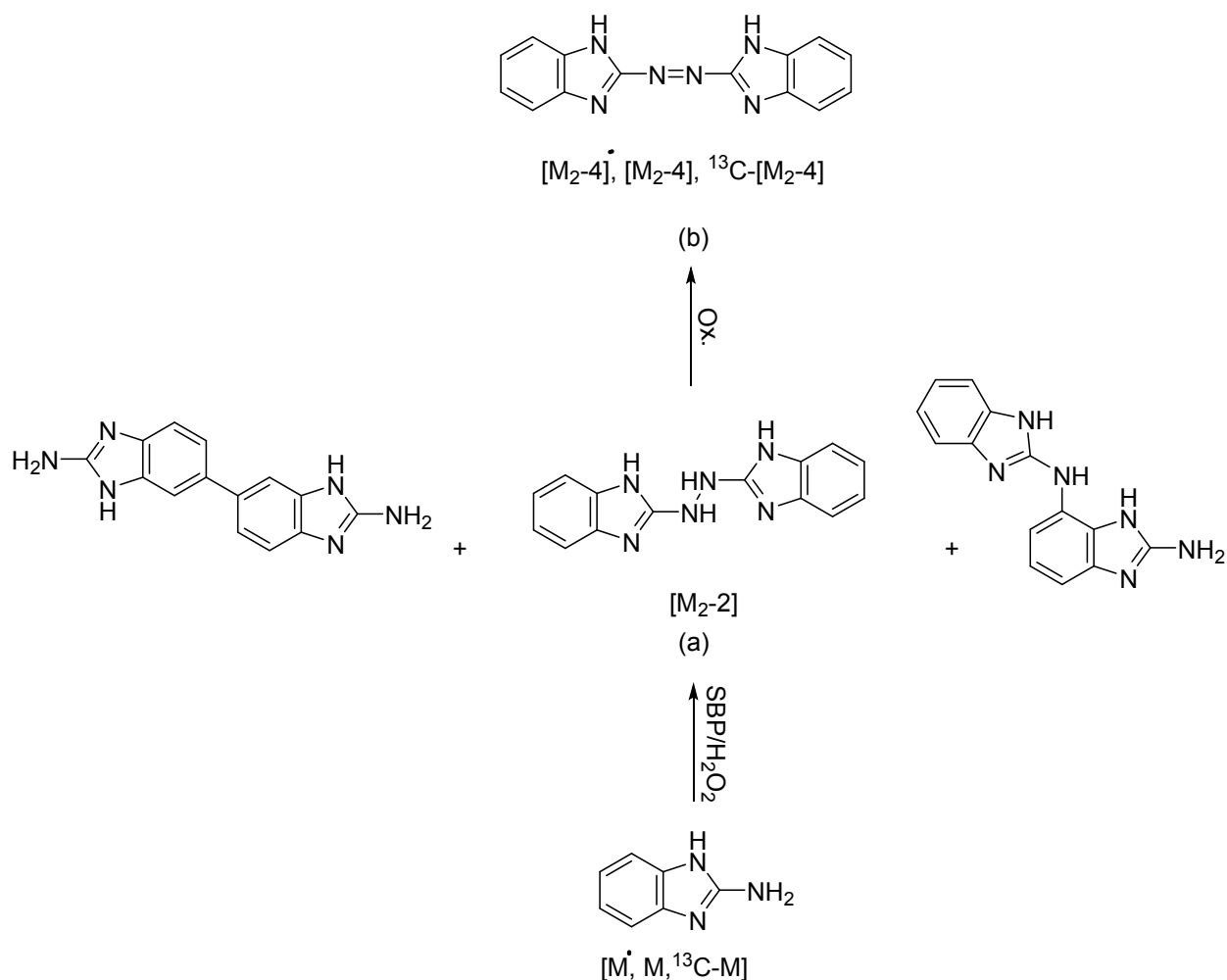


Figure S32. Proposed structures of oligomers found in enzymatic treatment of 2-ABI. Symbolic labels are defined in Figure 2 caption.

Pyrazoles

For 3-AP, ASAP-MS analysis showed both azo- and oxidized dimers in the supernatant of the enzymatic reaction. Based on the spin density map of 3-AP, radical C-C, N-C and N-N couplings are possible, indistinguishable by MS analysis, however, N-N coupling would lead to the observed azo-dimer, Figure 3(a), through the intermediate hydrazine. Although no direct evidence of the other two oxidative dimer isomers was observed either, Figure 3(b) and (c) structures could be derived from the C-C coupled oxidative dimer through consecutive loss of ammonia (or NH and H₂) and NH, respectively. Loss of ammonia is a common fragmentation

pattern of primary amines and to a lesser extent from secondary amines (Gross, 2006). Figures 3(d) and (e), bipyrazolyl structures, could be the result of consecutive loss of two NH from an oxidative dimer also formed through C-C coupling. Loss of NH from N-aminoazoles, specifically almost all N-aminopyrazoles, has been reported as the major fragmentation pattern (Kuzmenko and Pozharskii, 1992). Formation of oxygenated dimers such as Figures 3(f) and (g) further confirms the presence of oxidative and azo-dimers, respectively. In addition to the dimers, a mono-azo-trimer with two possible structures, shown in Figure 3(h), could result from further enzymatic oligomerization by N-N coupling of the free amino group of an oxidative dimer formed through C-C or C-N coupling, followed by oxidation. None of the above peaks were observed in the ASAP-MS spectrum of the precipitate of the 3-AP reaction with only a peak indicating loss of N₂ from an oxidative dimer shown in Figure 3(i). No plausible pathway for the formation of such structure can be suggested. Loss of N₂ from the standard is likely (Gross, 2006) but could not be confirmed due to low-mass range limitations of the instrument.

4-AAP

Enzymatic treatment of 4-AAP did not result in the formation of a precipitate; thus, the supernatant of the reaction was analyzed using ASAP-MS. The peaks matching the empirical formulae of a protonated azo-dimer (Figure S33) and its radical cation were observed. Although no peak directly indicating the presence of an oxidative dimer (a hydrazine) was found, an empirical formula related to an oxygenated or hydroxylated dimer was found. No evidence for oxidative dimers formed through C-C or C-N coupling was found, not surprising in view of the fact that such coupling would disrupt aromaticity of the pyrazole ring.

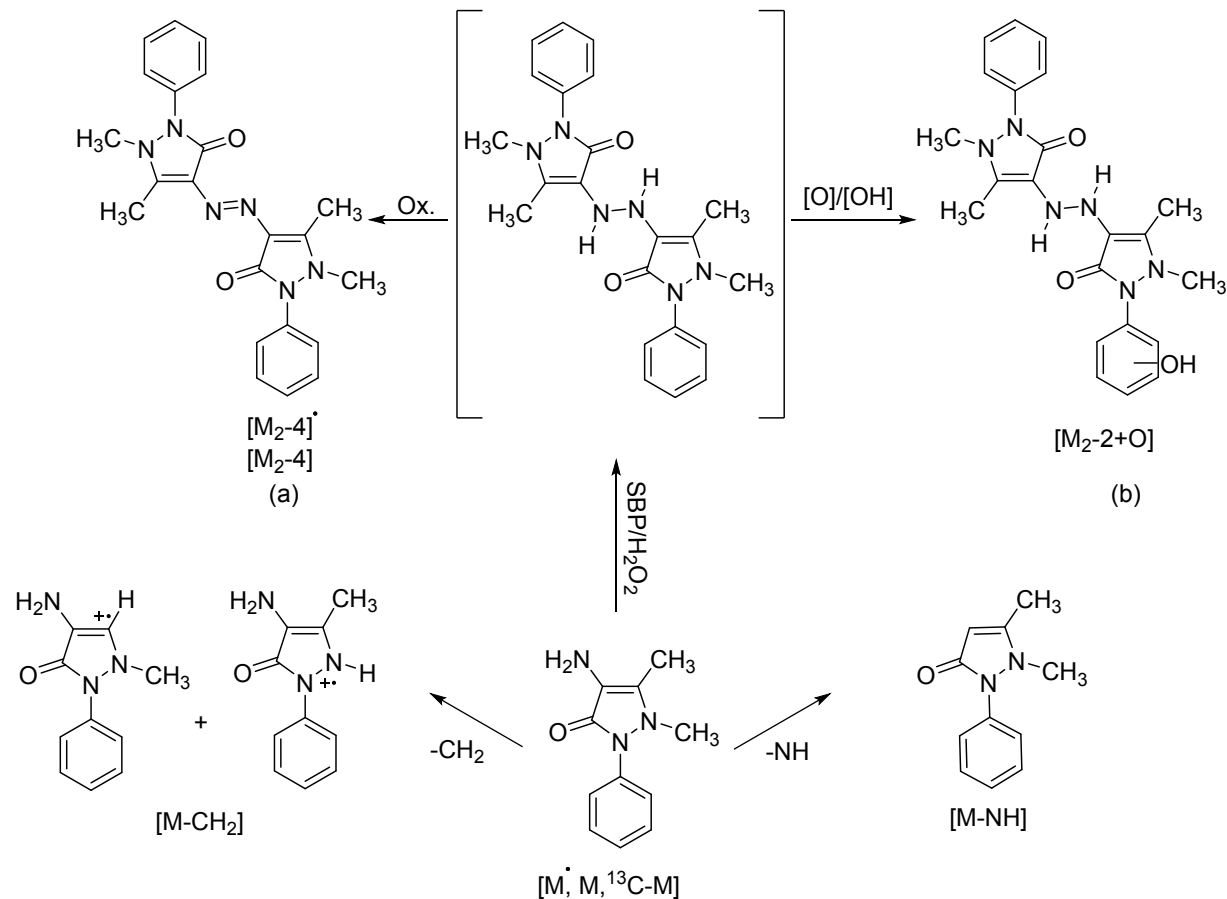


Figure S33. Proposed structures of oligomers found in enzymatic treatment of 4-AAP. Symbolic labels are defined in Figure 2 caption.

HOBT

In the ASAP-MS spectrum of the HOBT standard, peaks of radical cation and protonated substrate were observed. Based on spin density calculations, highest spin values are observed on oxygen and two of the nitrogen atoms. Thus, oxidative dimers through N-N, N-O and O-O coupling could be expected and good evidence was obtained for the O-O-coupled dimer, Figure 4(a). However, N-N and N-O coupling would lead to loss of aromaticity in one or both of the heterocyclic rings (intermediates drawn in Figure 4(a')) which could be overcome by facile dehydration; peaks consistent with subsequent transformation of such dehydration products were detected as follows. A series of peaks indicating loss and addition of oxygen possibly derived from an oxidative dimer generated by N-O or N-N coupling (Figure 4(c)) was observed in the supernatant. On the other hand, dimer-like structures lacking two nitrogens were observed. Loss of N₂ is a common fragmentation pattern for heterocyclics having 2 adjacent nitrogens.(Gross, 2006) Addition of oxygen to the above structures was also observed (Figures 4(d)-(h)). Thus, in terms of stable compounds, direct MS evidence is consistent with the oxidative dimer in Figure 4(a) and indirect evidence is consistent with the dimers in Figure 4(a'). MS analysis of the precipitate of HOBT reaction also showed the peaks observed in the supernatant, except the structure observed in Figure 4(h).

density calculation which indicates coupling through N-N, C-N or C-C would be possible through both nitrogens and the carbon in position 5. No literature on enzymatic polymerization of 2-AT was found but electrochemical polymerization in acetonitrile (Ciftci et al., 2011) and ammonium oxalate solution (Solmaz and Kardas, 2009) have been previously reported. FTIR, UV-vis and $^1\text{H-NMR}$ analysis of the polymer suggested that a radical cation is generated through the oxidation of the amino group of 2-AT. C-N coupling was believed to be the favored coupling route as no N=N stretching was observed in the infrared spectrum (Solmaz and Kardas, 2009; Yildirim and Kaya, 2012). In this work, the presence of azo-dimers was confirmed using ASAP-MS analysis. Formation of such products has also been reported for peroxidase-catalyzed oligomerization of aniline xenobiotics (Michail et al., 2013) and SBP-catalyzed oligomerization of 3-aminoquinoline (Mashhadi et al., 2019) and it is believed to be due to the autoxidation of the hydrazine oxidative dimer to the azo-compound (Karich et al., 2017). In addition to the oxidative and azo-dimers, a dimer-like structure with the empirical formula $[\text{M}_2-2-2\text{NH}]$, Figure S34 (d), was observed which could be due to the loss of both NH groups from the C-C linked oxidative dimer in Figure S34 (a). Although no peak indicating the presence of $[\text{M}_2-2-\text{NH}]$ was observed, loss of a second NH from such intermediate (Figure S34(c)) seems likely. Loss of NH during fragmentation of phenylhydrazines in mass spectrometry has been previously reported (Benoit and Holmes, 1969). Furthermore, two peaks suggesting the presence of an azo-trimer, $[\text{M}_3-6]$, and its ^{13}C isotope were also observed, Figure S34 (f). A hydrazine intermediate, Figure S34(e), would lead to the formation of azo-trimer.

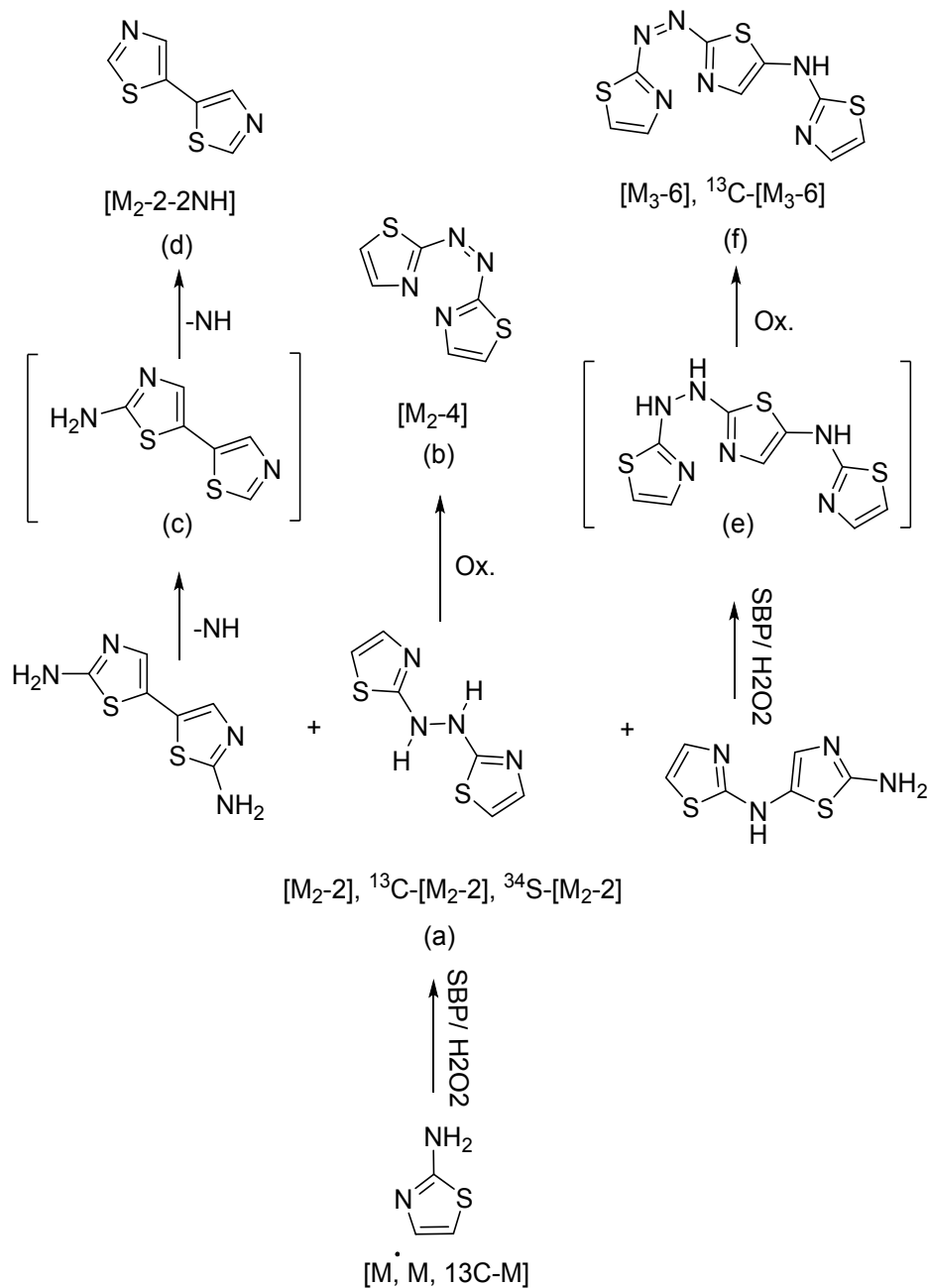


Figure S34. Proposed structures of oligomers found in enzymatic treatment of 2-AT. Symbolic labels are defined in Figure 2 caption.

2-ABT

The ASAP-MS analysis of 2-ABT (Figure S35) showed peaks attributed to the presence of radical cation $[M^{\bullet}]$, protonated standard $[M]$ and its ^{13}C and ^{34}S isotopes. Loss of HCN has been previously reported as one of the most common fragmentation patterns of benzothiazole (Millard

and Temple, 1968), with a peak indicating such fragmentation observed in the current work, Figure S35 (a). Benzothiazole derivatives (except the 2-mercapto-derivative) also undergo cleavage of their heteroaromatic ring during ESI-MS analysis resulting in formation of a peak at m/z 109 (Sadr-Arani et al., 2015). In this work, a lower intensity peak at m/z 109.010 seen during ASAP ionization of the standard, was believed to be due to consecutive loss of NH after HCN loss and is shown in Figure S35 (b). Additionally, the peak of protonated benzothiazole was also observed suggesting loss of NH group, $[M-NH]$, from the standard during the analysis. This result was confirmed by repeating the analysis using the ESI ionization method. ASAP analysis of enzymatically treated 2-ABT showed peaks confirming the presence of the protonated azo-dimer, $[M_2-4]$, and its ^{13}C and ^{34}S isotopes, Figure S35 (d), as observed above for 2-AT. Unlike 2-AT, previous electrochemical polymerization conducted on 2-ABT and 1H -NMR analysis of the products formed suggested the exocyclic nitrogen and C-6 as the preferred coupling sites (Yildirim and Kaya, 2012). Although no peak indicating the presence of hydrazine (Figure S35 (e)), or any other possible oxidative dimer was observed after 2-ABT treatment, two peaks indicating the presence of dimer-like structures (possibly C-C coupled) with consecutive loss of NH groups from an oxidative dimer, Figure S35 (f) and (g), suggest the presence of oxidative dimer intermediates with plausible structures shown in brackets.

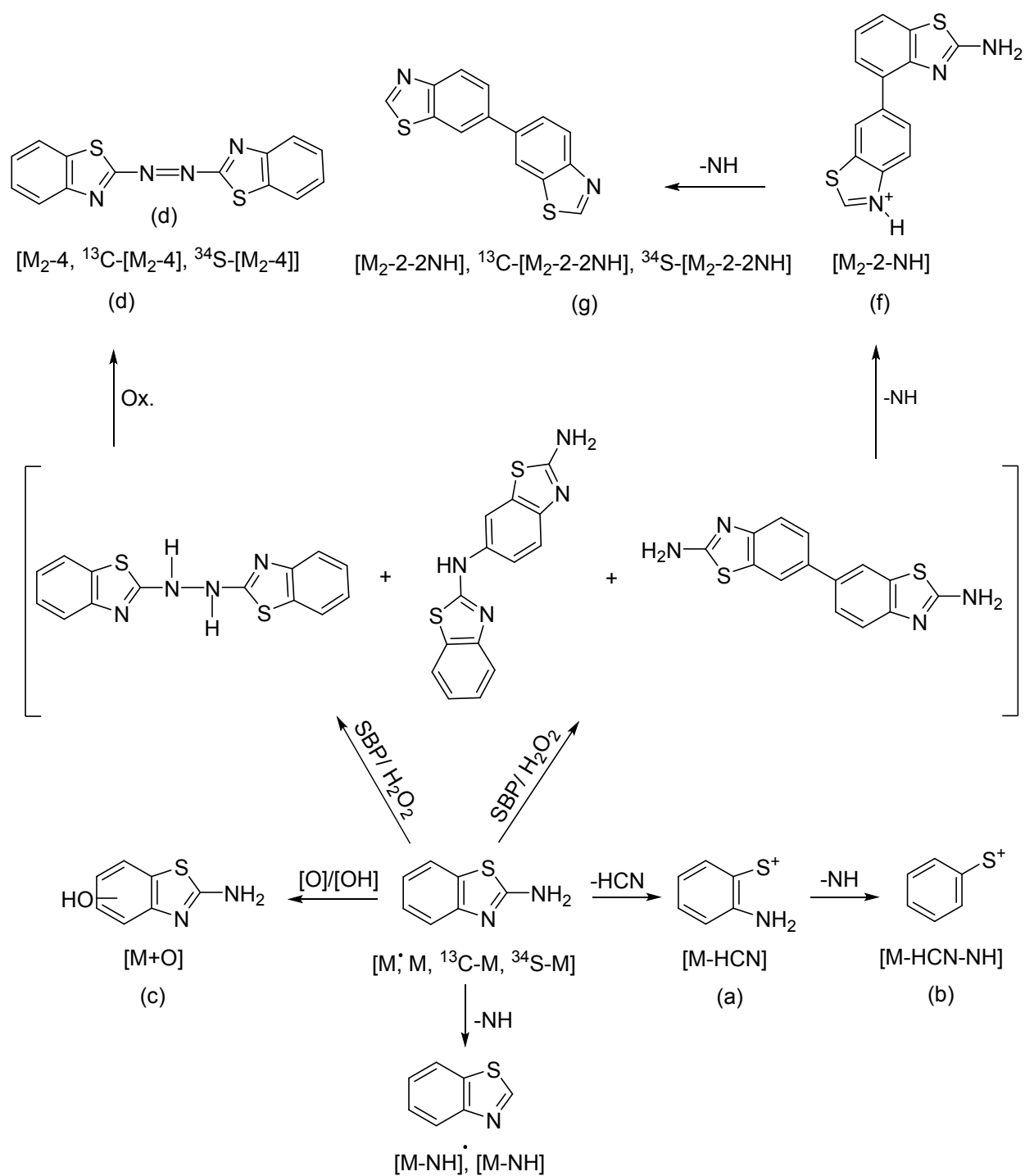


Figure S35. Proposed structures of oligomers found in enzymatic treatment of 2-ABT. Symbolic labels are defined in Figure 2 caption.

Pyrrole

The plausible pathways of oligomerization of pyrrole during enzymatic treatment are shown in Figure S36. Peaks of pyrrole molecular ion, protonated pyrrole and its ^{13}C isotope were observed during ASAP-MS analysis of the standard. In addition to pyrrole, a prominent peak suggesting the presence of oxygenated standard (possibly pyrrollin-n-one) was also observed. Analysis of the reaction mixture after enzymatic treatment showed mainly the evidence of protonated forms of the oxygenated trimers seen in Figures S36 (d-h). Evidently all three trimers are found to be oxygenated as previously seen for pyrrole standard. Oxygenation reactions are known to occur during direct analysis in real time and electrospray ionization as observed here during ASAP analysis (Madarshahian et al., 2017). Formation of oxygenation products during ASAP analysis of quinolines has been reported (Mashhadi et al., 2019). In addition to trimer and its oxidized products, peaks corresponding to presence of a tetramer and its oxygenated form were observed (Figures S36 (k) and (l)).

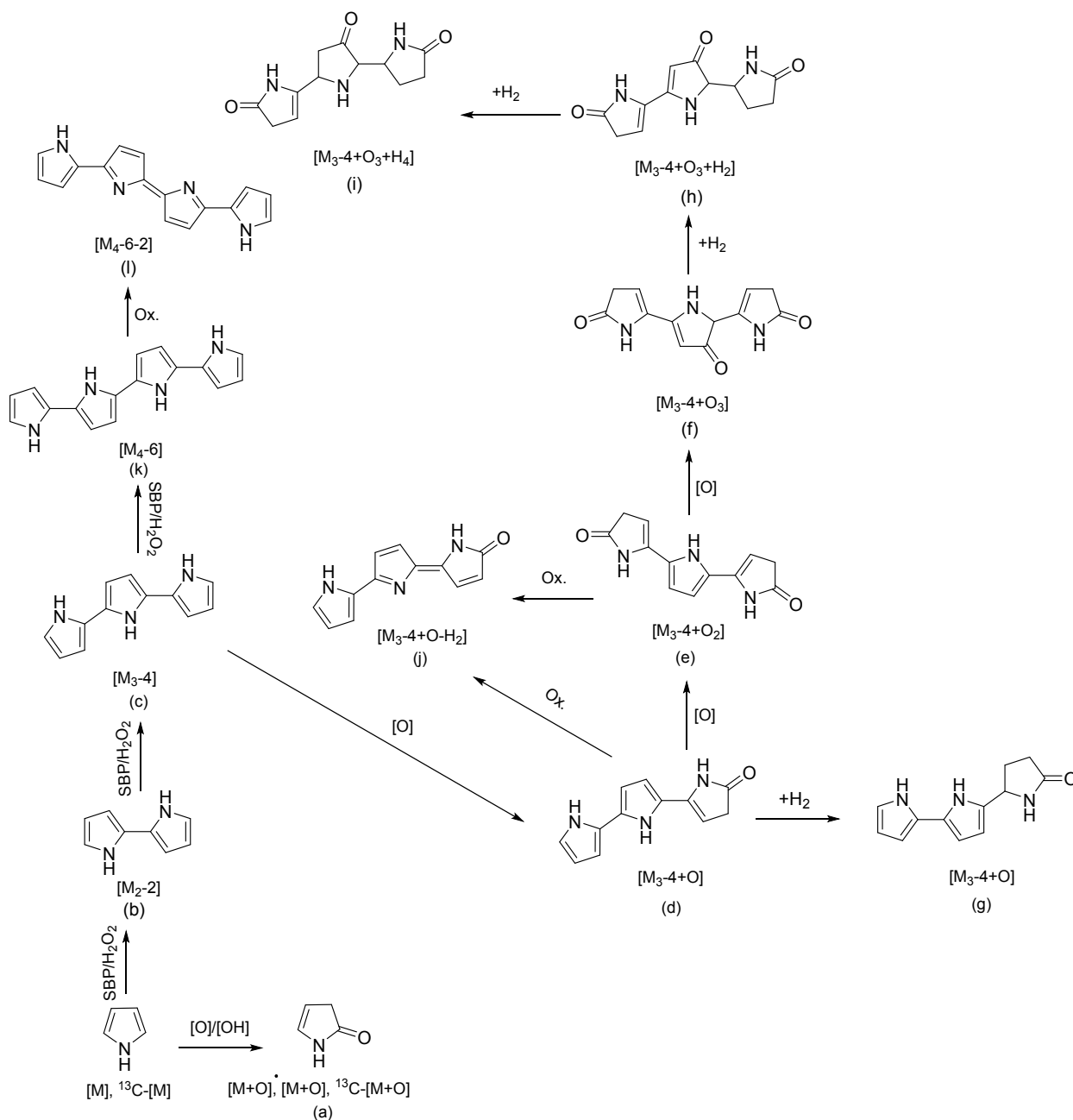


Figure S36. Proposed structures of oligomers found in enzymatic treatment of pyrrole. Symbolic labels are defined in Figure 2 caption.

Indole

In ASAP analysis of indole standard, the peak of indole radical cation $[M]^+$, protonated standard $[M]$ and its ^{13}C -isotope was observed. In addition, as reported previously (Powers, 1968), fragmentation of the parent ion through the loss of HCN and H_2CN was observed. Addition of

oxygen to the molecular ion led to the presence of an oxindole peak. Single and double oxygenation of terpendoles during positive-ion ESI- MS analysis had shown to be unpredictable as it happened only in some of them. Oxygenation was preferably observed at the indole protonation site of terpendoles (Hongo et al., 2014). Oxygenation of substrates and their enzymatically generated oligomers has been frequently observed during this study. ASAP analysis of treated indole showed strong peaks suggesting the presence of protonated isatin (Figure S37 (a)) and its ^{13}C isotope. Although isatin formation has been previously reported using cytochrome P450 (Gillam et al., 2000), such product was not expected by SBP treatment. In addition, peaks suggesting the presence of oxidative dimers, cyclic dimers and their oxidized and oxygenated products (Figures S37 (b, b', n, n', o')) were observed after enzymatic treatment. In addition to in-source oxygenation of substrate and products observed, uptake of enzymatically generated indolyl radical by the oxygen molecule during the reaction cannot be ruled out. Such addition has been reported for horseradish peroxidase oxidation of methylindole, leading to the formation of indigo- and indirubin-like structures (Ximenes et al., 2001). In this work, peaks attributed to the presence of indigo or indirubin with structures shown in Figure S37 (p') were observed. Based on the possible resonance structures which could be drawn for indolyl radical, there will be many possibilities for C-C, C-N, N-N coupling products. Formation of such compounds has been reported during cytochrome P450 oxidation of indole (Gillam et al., 2000). Further oligomerization of dimers generated was shown to result in formation of various trimers and tetramers along with their oxygenated products, Figure S38. Considering the molecular formula assigned to trimer peaks observed, cyclic conjugated structures with exceptional solubility such as triazatruxene or isotriazatruxene (10,15-Dihydro-5H-diindolo[3,2-a:3',2'-c]carbazole) (Li et al., 2016b), are expected.

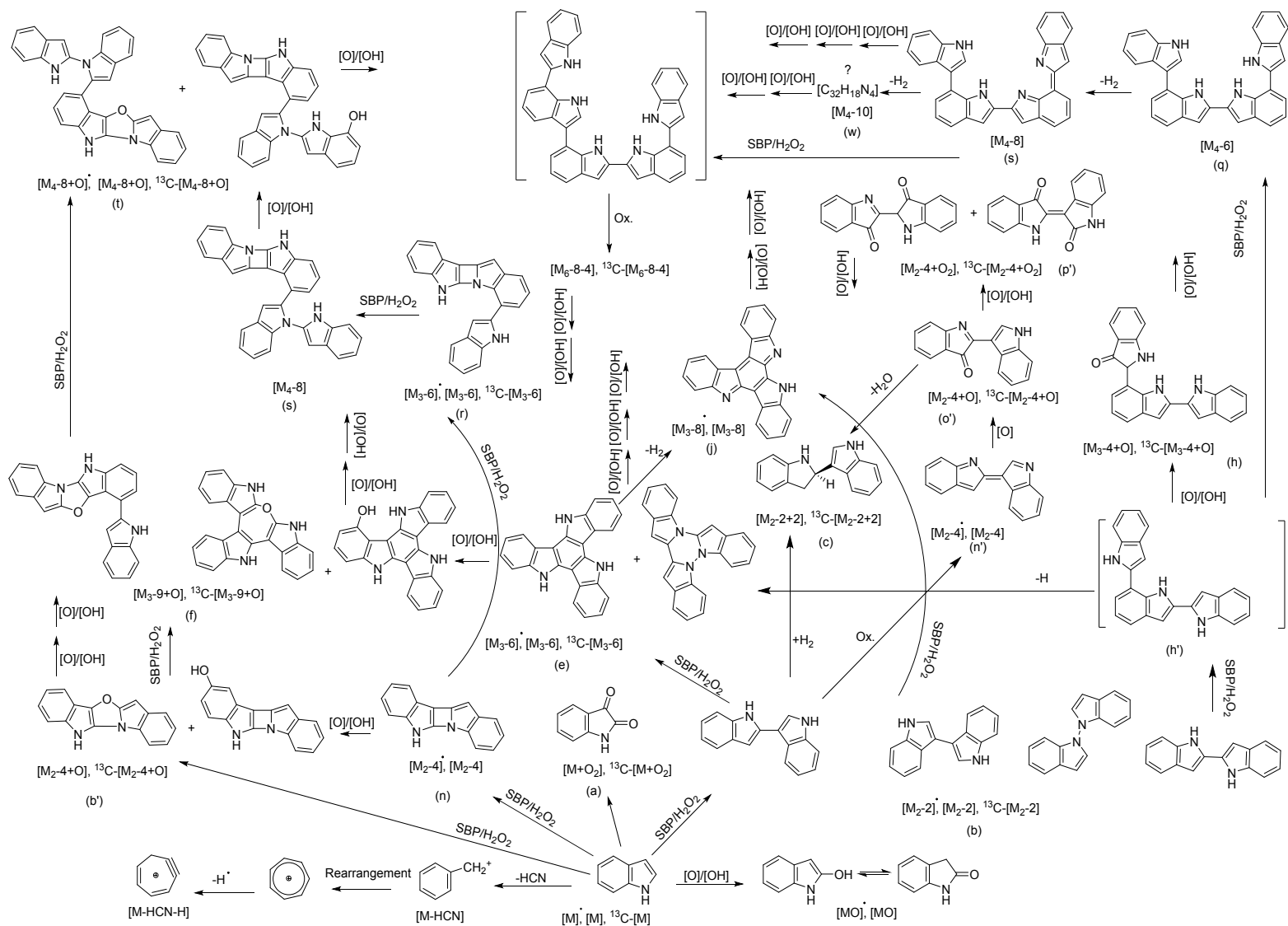


Figure S37. Proposed structures of oligomers found in enzymatic treatment of indole. Symbolic labels are defined in Figure 2 caption.

Benoit, F., Holmes, J., 1969. Mass spectra and fragmentation mechanisms of some nitrophenylhydrazines and nitrophenylhydrazones. *Can. J. Chem* 47, 3611-3621.

Çiftçi, H., Testereci, H.N., Öktem, Z., 2013. Preconcentration and electroanalysis of silver at Pt electrode modified with poly(2-aminothiazole). *Russian Journal of Electrochemistry* 49, 1160-1164.

Gillam, E.M., Notley, L.M., Cai, H., De Voss, J.J., Guengerich, F.P., 2000. Oxidation of indole by cytochrome P450 enzymes. *Biochemistry* 39, 13817-13824.

Gross, J.H., 2006. *Mass spectrometry: a textbook*. Springer Science & Business Media.

Karich, A., Ullrich, R., Scheibner, K., Hofrichter, M., 2017. Fungal unspecific peroxygenases oxidize the majority of organic EPA priority pollutants. *Front. Microbiol.* 8.

Kinsley, C., Nicell, J.A., 2000. Treatment of aqueous phenol with soybean peroxidase in the presence of polyethylene glycol. *Bioresour. Technol.* 73, 139-146.

Kuzmenko, V.V., Pozharskii, A.F., 1992. N-Aminoazoles. in: Katritzky, A.R. (Ed.). *Advances in Heterocyclic Chemistry*. Academic Press, pp. 85-231.

Li, C., Hsu, Y.-T., Hu, W.-W., 2016a. The regulation of osteogenesis using electroactive polypyrrole films. *Polymers* 8, 258.

Li, X.-C., Wang, C.-Y., Lai, W.-Y., Huang, W., 2016b. Triazatruxene-based materials for organic electronics and optoelectronics. *J. Mater. Chem.* 4, 10574-10587.

Lu, B., Li, Y., Xu, J., 2010. Electropolymerization study of benzothiophenes and characterization of novel poly(dibenzothiophene-S, S-dioxide). *Journal of Electroanalytical Chemistry* 643, 67-76.

Madarshahian, S., Pophristic, M., McEwen, C.N., 2017. Infrared atmospheric solids analysis probe (IR-ASAP) mass spectrometry for ambient analysis of volatile compounds without heated gas. *Anal. Methods* 9, 5009-5014.

Mashhadi, N., Taylor, K.E., Biswas, N., Meister, P., Gauld, J.W., 2019. Oligomerization of 3-substituted quinolines by catalytic activity of soybean peroxidase as a wastewater treatment. Product formation and computational studies. *Chem. Eng. J.* 364, 340-348.

Millard, B., Temple, A., 1968. High resolution mass spectrometry.—II Some substituted benzothiazoles. *J. Mass Spectrom.* 1, 285-294.

Mukhopadhyay, A., Jacob, L., Venkataramani, S., 2017. Dehydro-oxazole, thiazole and imidazole radicals: insights into the electronic structure, stability and reactivity aspects. *Physical Chemistry Chemical Physics* 19, 394-407.

Sadr-Arani, L., Mignon, P., Chermette, H., Abdoul-Carime, H., Farizon, B., Farizon, M., 2015. Fragmentation mechanisms of cytosine, adenine and guanine ionized bases. *Phys. Chem. Chem. Phys.* 17, 11813-11826.

Solmaz, R., Kardas, G., 2009. Electrochemical synthesis and characterization of poly-2-aminothiazole. *Prog. Org. Coat.* 64, 81-88.

Ximenes, V.F., Campa, A., Catalani, L.H., 2001. The oxidation of indole derivatives catalyzed by horseradish peroxidase is highly chemiluminescent. *Arch. Biochem. Biophys.* 387, 173-179.

Yildirim, M., Kaya, I., 2012. Electrochemical syntheses and characterizations of poly(2-aminobenzothiazole)s. *Synth. Met* 162, 834-842.

Yurtsever, E., Yurtsever, M., 1999. A theoretical study of structural defects in conjugated polymers. *Synth. Met.* 101, 335-336.

Yurtsever, M., Yurtsever, E., 2002. A DFT study of polymerization mechanisms of indole. *Polymer* 43, 6019-6025.